Advanced Optical Materials

ADVANCED OPTICAL MATERIALS
www.advopticalmat.de

RESEARCH ARTICLE OPEN ACCESS

Exciton Radiative Lifetimes in Hexagonal Diamond Ge and Si_xGe_{1-x} Alloys

Michele Re Fiorentin[1] | Michele Amato[2] | Maurizia Palummo[3]

[1]Department of Applied Science and Technology, Politecnico di Torino, Torino, Italy | [2]CNRS, Laboratoire de Physique des Solides, Université Paris-Saclay, Orsay, France | [3]INFN and Dipartimento di Fisica, Università degli studi di Roma "Tor Vergata", Rome, Italy

Correspondence: Michele Re Fiorentin (michele.refiorentin@polito.it)

Received: 17 December 2025 | **Revised:** 25 March 2026 | **Accepted:** 13 April 2026

ABSTRACT

Recent reports of strong room-temperature photoluminescence in hexagonal diamond (2H) germanium stand in marked contrast to theoretical predictions of very weak band-edge optical transitions. Here, we address radiative emission in 2H-Ge and related materials through a comprehensive investigation of their excitonic properties and radiative lifetimes, performing Bethe–Salpeter calculations on pristine and uniaxially strained 2H-Ge, 2H-Si_xGe_{1-x} alloys with $x = 1/6, 1/4, 1/2$, and wurtzite GaN as a reference. Pristine 2H-Ge features sizable exciton binding energies (~ 30 meV) but extremely small dipole moments, yielding radiative lifetimes above 10^{-4} s. Alloying with Si reduces the lifetime by nearly two orders of magnitude, whereas a 2% uniaxial strain along the c axis induces a band crossover that strongly enhances the in-plane dipole moment of the lowest-energy exciton and drives the lifetime down to the nanosecond scale. Although strained 2H-Ge approaches the radiative efficiency of GaN, its much lower exciton energy prevents a full match. These results provide the missing excitonic description of 2H-Ge and 2H-Si_xGe_{1-x}, demonstrating that, even when excitonic effects are fully accounted for, the strong photoluminescence reported experimentally cannot originate from the ideal crystal.

1 | Introduction

The hexagonal diamond phase (lonsdaleite, 2H in the Ramsdell notation [1]) of germanium has recently been grown in a variety of structures, from nanowires [2–4] and nanobranches [5–7], to quantum wells [8, 9]. The successful stabilization of this metastable phase in nanostructures has established 2H-Ge as a promising group-IV material for optoelectronic applications. The strong room-temperature photoluminescence (PL) observed by Fadaly et al. [4] in 2H-Ge and 2H-Si_xGe_{1-x} nanowires further suggested the possibility of an intrinsic, efficient light emitter within this polytype. This result generated considerable interest by revealing an unexpected route to strong optical emission in group-IV materials, a class traditionally limited by the indirect bandgap of the cubic diamond phase. Achieving optical emitters, lasers, detectors, and integrated photonic components remains a long-standing goal in the development of silicon photonics [10–14]. In this context, the apparent emergence of a direct-gap light emitter based solely on group-IV elements has renewed both scientific and technological interest in 2H-Ge.

Despite this excitement, theoretical analyses revealed inconsistencies between the reported strong PL and the predicted optical properties of 2H-Ge [6, 15]. First-principles calculations consistently show that the fundamental Γ-point transition in 2H-Ge carries extremely weak oscillator strength. Rödl et al. [16] demonstrated that the dipole matrix element between the valence-band maximum (VBM) and the conduction-band minimum (CBm) at Γ is strongly suppressed, classifying 2H-Ge as a pseudo-direct semiconductor. Optical absorption and electron energy-loss spectroscopy (EELS) further confirmed the absence of pronounced features at the electronic band edge [6, 16],

---

This is an open access article under the terms of the Creative Commons Attribution License, which permits use, distribution and reproduction in any medium, provided the original work is properly cited.

© 2026 The Author(s). *Advanced Optical Materials* published by Wiley-VCH GmbH

revealing a nearly "dark" transition. Additional first-principles works [17, 18] have reached similar conclusions, suggesting that the reported PL is not intrinsic and may instead arise from extrinsic mechanisms such as defects, morphology, or local strain fields [4, 15, 19, 20].

Existing optical calculations on 2H-Ge have primarily focused on the independent-particle (IP) regime [16, 18], evaluating dipole transitions and PL assuming free electron–hole recombination. While such an approach captures essential characteristics, including the vanishing dipole matrix elements at the Γ point, it neglects exciton formation and their impact on radiative recombination. Previous analyses have generally assumed a small exciton binding energy, by analogy with cubic Ge (3C-Ge), where $E_b \sim 4$ meV [21], implying that excitonic effects would be negligible at finite temperature and that an IP description would suffice. Hence, despite the growing interest in polytypic group-IV materials, a comprehensive study of the excitonic properties of 2H-Ge, SiGe alloys, and strained hexagonal variants has so far been lacking.

In this work, we aim to fill this gap by performing ab initio calculations based on Density Functional Theory (DFT) and the Bethe-Salpeter equation (BSE) on pristine 2H-Ge, on 2H-Ge under uniaxial strain along the c axis, a strategy previously shown to modify band ordering and enhance light emission [17], and on representative 2H-Si_xGe_{1-x} alloys, with $x = 1/6, 1/4, 1/2$. We compute absorption spectra, exciton binding energies, dipole moments, and intrinsic radiative lifetimes, thereby providing a comprehensive excitonic description of these systems. This provides the first excitonic investigation of 2H-Ge–based materials, going beyond the IP analyses available so far and supplying an intrinsic optical benchmark long missing in this field.

We find sizable exciton binding energies (∼30 meV in pristine 2H-Ge), confirming that the excitonic picture is the most appropriate to describe the optical properties of these systems. Our results demonstrate that pristine 2H-Ge has intrinsically very long radiative lifetimes, exceeding 10^{-4} s at low temperature, highlighting its pseudo-direct character. Alloying with Si moderately enhances the dipole strength by lifting symmetry-imposed constraints, whereas uniaxial strain produces a far more dramatic enhancement, reducing the radiative lifetime by more than five orders of magnitude and approaching the nanosecond regime. The strained system displays dipole moments and radiative efficiencies that approach those of wurtzite GaN, our reference efficient wide-bandgap emitter.

By combining exciton binding energies, dipole moments, oscillator strengths, and radiative lifetimes, our analysis provides a complementary theoretical perspective that reinforces previous findings of intrinsically weak optical activity in 2H-Ge. Our results substantiate the conclusion that the strong PL observed experimentally is likely driven by extrinsic mechanisms, while identifying strain engineering as a viable and highly effective route to enhance intrinsic light emission in 2H-Ge and reconcile theory and experimental results. The strain levels required to induce such effects are not unrealistic in nanowire geometries, where large elastic deformations can be sustained, with tensile strain approaching ∼1.5% reported in Ge nanowires and even larger values achievable, more generally, in semiconductor nanowires [22, 23].

The article is organized as follows. In Section 2, we describe the computational methods employed for the calculation of the electronic and excitonic properties; in Section 3 we present our results on the materials and their exciton radiative lifetimes. Finally, in Section 4 we summarize our findings and draw our conclusions.

2 | Methods

Ground-state calculations were carried out within plane-wave DFT, as implemented in the Quantum ESPRESSO code [24–26], with norm-conserving pseudopotentials, the PBEsol functional [27], and an 80 Ry kinetic-energy cutoff. Equilibrium structures were obtained through variable-cell optimization with increased cutoff value.

To assess the behavior of hexagonal diamond SiGe alloys, we considered representative configurations built in a hexagonal rotated $\sqrt{3} \times \sqrt{3} \times 2$ supercell containing 24 atoms. This size allowed us to introduce compositional disorder without resorting to substantially more expensive larger supercells. We focused on Si_xGe_{1-x} alloys with $x = 1/6, 1/4, 1/2$, where atomic randomness was generated through the special quasi-random structure (SQS) method [28, 29], which reproduced, already for relatively small cells, the radial correlation functions of an ideal random alloy. This model did not capture the full statistics of the alloys, which would require ensemble approaches or larger cluster sets such as those used in ref. [18]. Instead, it served as a controlled, representative example to illustrate the effects on the radiative lifetime of mixing Si and Ge in the hexagonal phase. More details on the optimized structures are reported in Section S1.

To reduce the computational cost while obtaining reliable electronic band structures of 2H-Ge and related systems, we employed a J-parameter correction within the Liechtenstein formalism of DFT + U + J [30]. In this scheme, the J term introduced an on-site exchange interaction on the Ge 4p orbital subspace, which predominantly forms the valence-band edge. This adjustment lowers the energy of the p-derived valence states relative to the largely s-like conduction states, thereby opening the bandgap. As a result, a finite positive gap between the valence and conduction bands of 2H-Ge was recovered, whereas standard DFT incorrectly predicts a negative bandgap. The bandgap could be tuned to match experimental and theoretical reference values by varying the J parameter; further details on its optimization are provided in Figure S2a.

We stress that the J values used here are effective parameters within the projector-defined DFT+J scheme, calibrated to reproduce hybrid-functional bandgaps and band-edge dispersions. In this work, they were employed as a computational device to reduce the overall computational cost, without assigning them a direct interpretation in terms of physical Hund's exchange parameters [31].

21951071, 0, Downloaded from https://advanced.onlinelibrary.wiley.com/doi/10.1002/adom.71234 by Cochraneltalia, Wiley Online Library on [16/05/2026]. See the Terms and Conditions (https://onlinelibrary.wiley.com/terms-and-conditions) on Wiley Online Library for rules of use; OA articles are governed by the applicable Creative Commons License

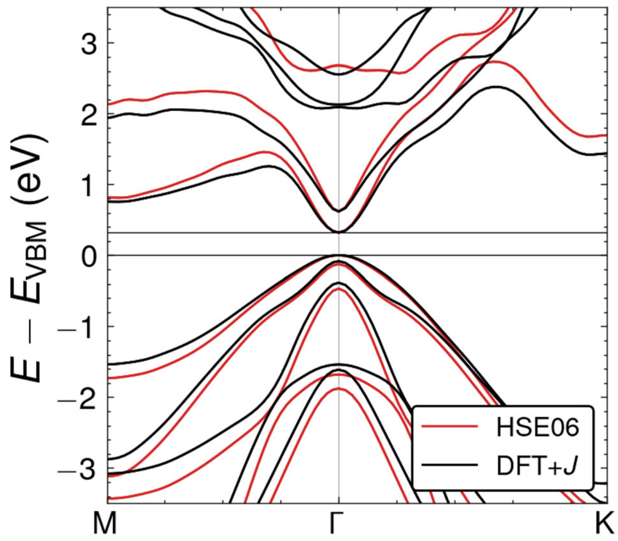

FIGURE 1 | Electronic band structure of 2H-Ge near the band extrema, computed with the HSE06 hybrid functional (black lines) and within the DFT+J method, with $J = 23$ eV (red lines).

In Figure 1, we show the band structure of 2H-Ge computed with the Heyd-Scuseria-Ernzerhof range-separated hybrid functional (HSE06) [32] (black lines) and with DFT+J, using $J = 23$ eV applied to the Ge 4p orbitals and no Hubbard U correction (red lines).

The chosen value of J reproduces the HSE06 bandgap $E_g = 0.32$ eV, consistent with previously reported values [6, 16, 33, 34], and yields a band structure in close agreement with the hybrid-functional result, in particular near the band extrema. This approach delivers HSE06-level accuracy at a fraction of the computational cost, enabling dense Brillouin-zone (BZ) sampling that would be impractical with hybrid functionals.

Throughout this work, the electronic band structures of 2H-Ge were computed using the $J = 23$ eV correction applied to the Ge 4p orbitals. For the 2H–$\mathrm{Si}_{1/6}\mathrm{Ge}_{5/6}$ and 2H–$\mathrm{Si}_{1/4}\mathrm{Ge}_{3/4}$ alloys, a larger value of $J = 40$ eV is required to match the corresponding HSE06 gap at that composition, reflecting the different local chemical environment in the alloy. For the Si-rich alloy 2H-$\mathrm{Si}_{1/2}\mathrm{Ge}_{1/2}$, a $J = 40$ eV correction is also applied to the Si 3p orbitals to match the HSE06 bandgap. See Figure S2b,c, for more details. All calculations include spin–orbit coupling (SOC).

The electronic structures served as the starting point for the optical-property calculations, obtained by solving the BSE with the YAMBO code [35, 36], and the optimized diagonalization routines available in its Lumen branch [37]. For 2H-Ge, we sample the BZ using a $21 \times 21 \times 14$ k-point grid, yielding 606 k-points in the irreducible BZ (6174 in the full BZ). We included 80 bands in the static screening, and applied a 2 Ry cutoff on the screened interaction. Additional details on the convergence of the k-point mesh, the number of bands included in the dielectric screening and the size of the static screening matrix are reported in the Figure S3a,b. The BSE kernel was built using six valence and four conduction bands, accounting for SOC. For the GaN benchmark, we started from the plain DFT band structure corrected with a scissor shift to reproduce the HSE06 bandgap, and employed analogous parameters for the BSE kernel.

The diagonalization of the Bethe-Salpeter Hamiltonian yields the exciton dipole moment of state S,

$$\mu_{S,\alpha} = \sum_{cv\mathbf{k}} w_{\mathbf{k}} A^S_{cv\mathbf{k}} \langle c\mathbf{k} | r_\alpha | v\mathbf{k} \rangle \tag{1}$$

in the length gauge, where $A^S_{cv\mathbf{k}}$ is the exciton eigenvector of state S, and α denotes the in-plane ($\perp c$) or out-of-plane ($\parallel c$) components.

The dipole moment also provides the dimensionless oscillator strength of exciton S,

$$f_{S,\alpha} = \frac{2m_0 E_S}{\hbar^2 e^2} |\mu_{S,\alpha}|^2 \tag{2}$$

where m_0 is the electron rest mass and E_S is the energy of exciton S. Exciton dipole moments enter the radiative lifetime of state S as given by [38, 39],

$$\tau_S(T) = \left(\frac{2M_{\perp c}^{2/3} M_{\parallel c}^{1/3} c^2 k_B T}{E_S^2} \right)^{3/2} \times \frac{\varepsilon_0 \hbar V}{\sqrt{\pi \varepsilon_{\perp c}} e^2 \left[\left(\frac{2\varepsilon_{\parallel c}}{3\varepsilon_{\perp c}} + 2 \right) |\mu_{S,\perp c}|^2 + \frac{8}{3} |\mu_{S,\parallel c}|^2 \right]} \tag{3}$$

where V is the simulation-cell volume, and $M_{\perp c}$, $\varepsilon_{\perp c}$, and $M_{\parallel c}$, $\varepsilon_{\parallel c}$ are the exciton mass and the optical dielectric constant for the in-plane and out-of-plane directions, respectively. The exciton effective masses entering Equation (3) are approximated as the sum of the electron and hole effective masses along the corresponding crystallographic directions. The carrier effective masses were extracted from the DFT+J band structure by fitting the band dispersion near the extrema using the `effmass` Python package [40]. The overall radiative lifetime of the material at temperature T is further obtained through a thermal average on the excitonic states [41],

$$\langle \tau \rangle (T) = \left(\frac{\sum_S 1/\tau_S(T) e^{-E_S/k_B T}}{\sum_S e^{-E_S/k_B T}} \right)^{-1} \tag{4}$$

Equation (3) assumes a Maxwell–Boltzmann distribution of the exciton center-of-mass momenta (CMM), i.e., that CMM states are rapidly redistributed by scattering (phonons, disorder) so that the light cone remains thermally populated. Under this approximation $\tau_S(T) \propto T^{3/2}$, which formally vanishes as $T \to 0$. Yet, this low-temperature limit is not physical: once scattering into the light cone freezes out (below the light-cone energy scale, $\lesssim 1$ K), the model ceases to apply and the actual lifetime increases rather than going to zero, since excitons with zero CMM cannot radiatively recombine in 3D solids due to momentum conservation [38]. All temperatures considered here lie above this low-temperature crossover. We also noted that radiative lifetimes computed within the IP approximation [4, 16, 42, 43] do not include this light-cone constraint and therefore remain

21951071, 0, Downloaded from https://advanced.onlinelibrary.wiley.com/doi/10.1002/adom.71234 by Cochraneitalia, Wiley Online Library on [16/05/2026]. See the Terms and Conditions (https://onlinelibrary.wiley.com/terms-and-conditions) on Wiley Online Library for rules of use; OA articles are governed by the applicable Creative Commons License

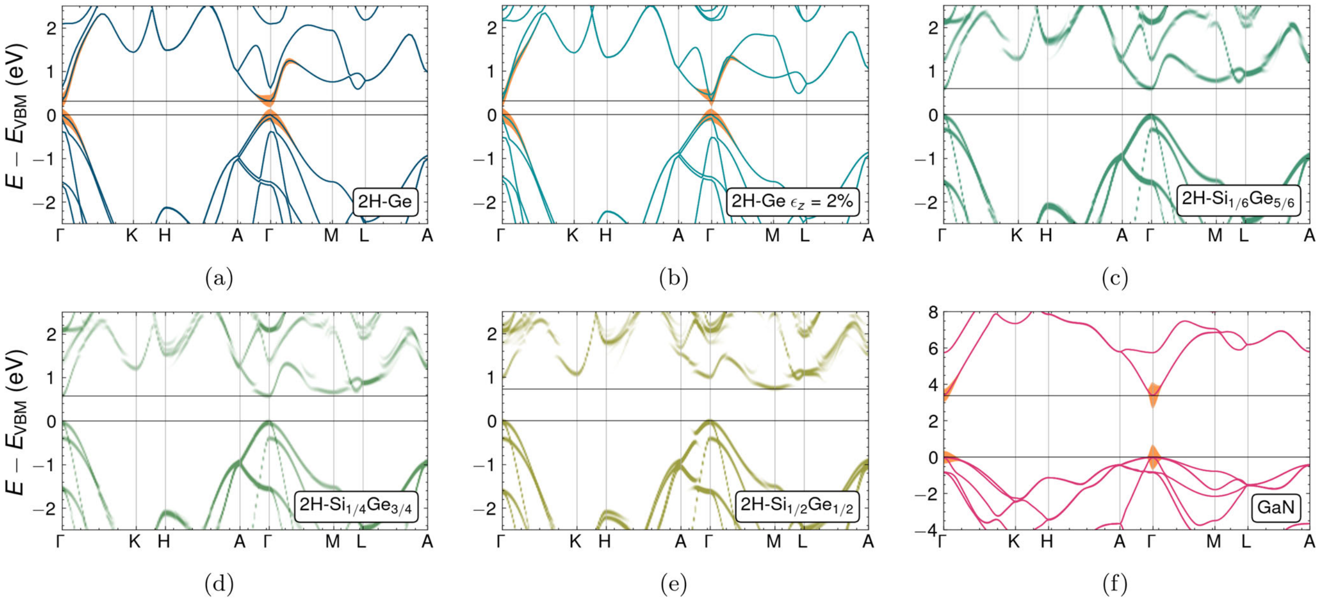

(a) (b) (c) (d) (e) (f)

FIGURE 2 | Band structures of the studied materials: (a) pristine 2H-Ge, (b) 2H-Ge under $\epsilon_z = 2\%$ uniaxial strain along the *c* axis, (c) 2H-Si$_{1/6}$Ge$_{5/6}$ alloy, unfolded onto the 2H-Ge BZ, (d) 2H-Si$_{1/4}$Ge$_{3/4}$ alloy, unfolded, (e) 2H-Si$_{1/2}$Ge$_{1/2}$ alloy, unfolded, (f) GaN. The orange shading highlights the electronic states contributing to the lowest-energy exciton state. Horizontal lines mark the electronic bandgaps.

TABLE 1 | Electronic structure parameters. Bandgaps E_g are in eV, and effective masses are expressed in units of the electron rest mass. For 2H-Si$_{1/2}$Ge$_{1/2}$, the direct gap at the Γ point and the electron effective masses at the *M* point are reported in brackets.

	E_g	$m^*_{h,\perp c}$	$m^*_{h,\parallel c}$	$m^*_{e,\perp c}$	$m^*_{e,\parallel c}$
2H-Ge	0.32	0.147	0.488	0.090	1.160
2H-Ge $\epsilon_z = 2\%$	0.32	0.119	0.499	0.038	0.031
2H-Si$_{1/6}$Ge$_{5/6}$	0.60	0.098	0.531	0.097	1.088
2H-Si$_{1/4}$Ge$_{3/4}$	0.58	0.121	0.698	0.097	1.774
2H-Si$_{1/2}$Ge$_{1/2}$	0.67	0.226	0.505	0.137	0.698
	(1.00)			(0.122)	(0.146)
GaN	3.40	0.164	2.418	0.144	0.161

finite as $T \to 0$. The excitonic lifetimes evaluated here describe a different regime where momentum-conserving recombination is governed by the CMM distribution and exhibits the characteristic $T^{3/2}$ dependence.

3 | Results and Discussion

3.1 | Electronic Structure

The electronic band structure of 2H-Ge obtained with the DFT+*J* method is shown in Figure 2a. The orange shading highlights the electronic states that contribute most to the lowest excitonic state. The lowest-energy transitions occur near the Γ point, from the VBM to the CBm. These transitions dominate the radiative properties of the material and are known to be particularly weak [18]. The bandgap and the effective masses of electrons at the CBm and of holes at the VBM, both along *c* (Γ→*A*) and perpendicular to *c* (Γ→*M*), are reported in Table 1, in good agreement with previous results [17].

Figure 2b shows the band structure of 2H-Ge under 2% uniaxial strain along the *c* axis. As discussed in ref. [18], strain induces a crossover between the Γ^-_{7c} state (CBm+1 in pristine 2H-Ge) and the Γ^-_{8c} state (CBm in the unstrained system), which become, respectively, CBm and CBm+1 in the strained material. The value of 2% strain should be regarded as a representative case where the band crossover is clearly established. Previous theoretical work indicates that the crossover may occur already at slightly lower strain ($\sim 1-1.5\%$), depending on the computational approach [18, 44]. Although the bandgap changes only marginally, this crossover strongly affects the optical response: the lowest-energy exciton becomes dominated by much stronger optical transitions. The electron effective masses at the band edges (Table 1) are significantly reduced compared to the unstrained case.

The band structures of the 2H-Si$_x$Ge$_{1-x}$ alloys, unfolded onto the 2H-Ge BZ, are shown in Figure 2c–e. In agreement with previous calculations [45], for $x = 1/6$ and $1/4$, the alloys retain a direct gap, which increases to about 0.6 eV, while for $x = 1/2$ the bandgap is indirect between the Γ and the *M* points, see also Table 1. The

21951071, 0, Downloaded from https://advanced.onlinelibrary.wiley.com/doi/10.1002/adom.71234 by CochraneItalia, Wiley Online Library on [16/05/2026]. See the Terms and Conditions (https://onlinelibrary.wiley.com/terms-and-conditions) on Wiley Online Library for rules of use; OA articles are governed by the applicable Creative Commons License

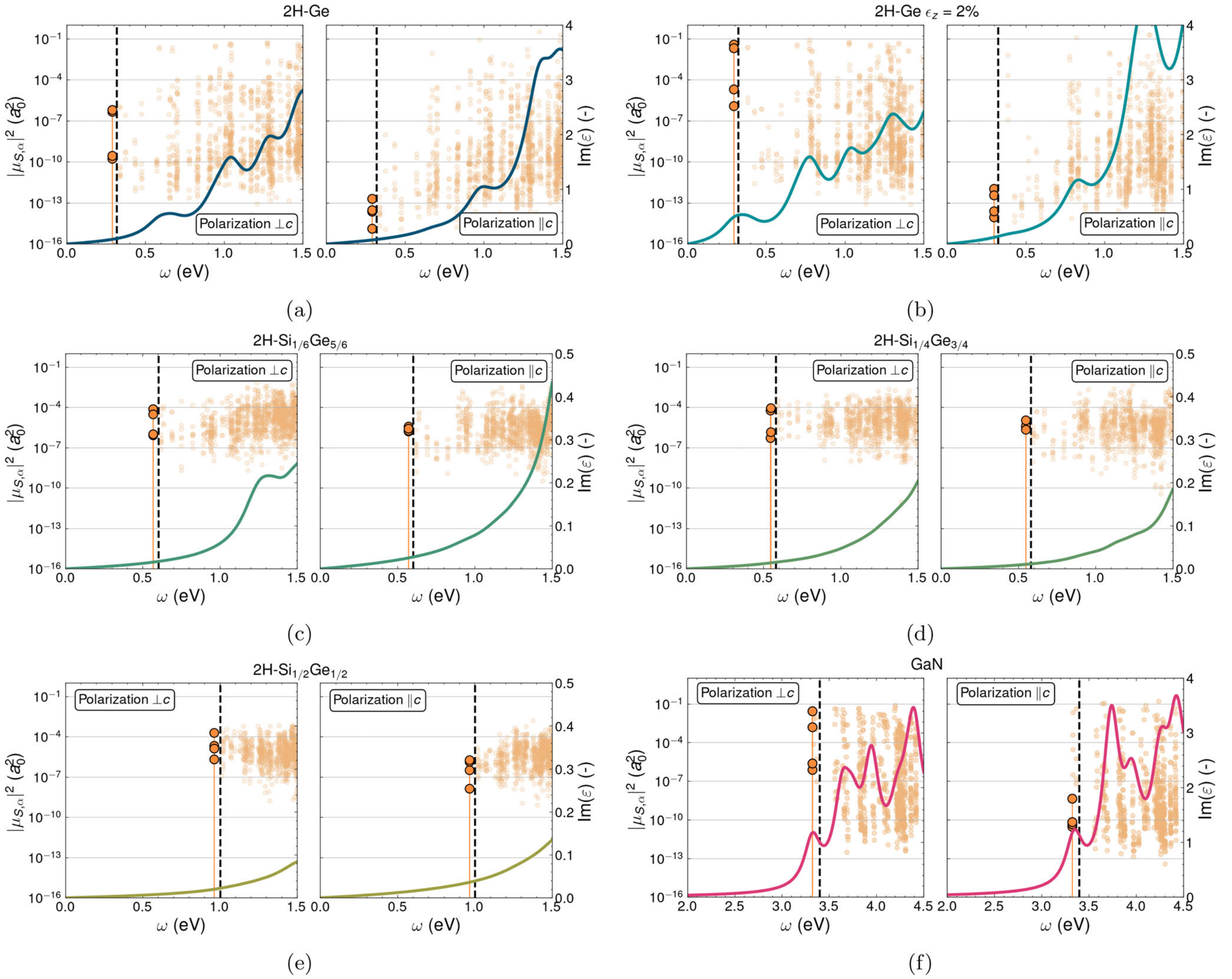

FIGURE 3 | Absorption spectra, Im(ε), and squared moduli of the exciton dipole moments, $|\mu_{S,\alpha}|^2$, in units of the Bohr radius squared, for 2H-Ge in panel (a), 2H-Ge under $\epsilon_z = 2\%$ uniaxial strain in (b), the 2H-Si$_{1/6}$Ge$_{5/6}$ alloy in (c), the 2H-Si$_{1/4}$Ge$_{3/4}$ alloy in (d), the 2H-Si$_{1/2}$Ge$_{1/2}$ alloy in (e), and GaN in (f). For each material, results are shown for in-plane ($\perp c$) and out-of-plane ($\parallel c$) light polarizations. The dashed vertical lines indicate the electronic bandgaps.

overall dispersions remain quite close to that of pristine 2H-Ge, except for the CBm+1 state, which is pushed upward in energy with increasing Si content, to roughly 1.2, 1.5, and 1.8 eV above the VBM for $x = 1/6$, $1/4$, and $1/2$, respectively.

Finally, Figure 2f displays the band structure of GaN, used here as a benchmark. GaN features a much larger bandgap, with both VBM and CBm located at Γ, and the lowest-energy exciton dominated by the zone-center transitions highlighted in the figure. The computed effective masses, reported in Table 1, are in good agreement with previous results in the literature [46].

3.2 | Exciton Dipoles and Oscillator Strengths

The solution of the BSE provides direct access to the optical absorption spectrum via the imaginary part of the dielectric function, Im(ε), as well as to the excitonic fine structure, including excitation energies and dipole moments of the individual states, Equation (1). Owing to the anisotropy of the hexagonal lattice, we distinguish between light polarized in the basal plane ($\perp c$) and along the c axis ($\parallel c$). The corresponding absorption spectra and squared moduli of the exciton dipole moments $|\mu_{S,\alpha}|^2$ for pristine 2H-Ge are shown in Figure 3a. The solid lines report Im(ε_α) for in-plane (left panel) and out-of-plane (right panel) polarized light, while the orange dots indicate the energies and the $|\mu_{S,\alpha}|^2$, expressed in units of the Bohr radius squared (a_0^2), for all excitonic states obtained from the BSE. The lowest-energy excitons are highlighted for clarity.

The lowest-energy exciton state is fourfold degenerate, originating from transitions between the twofold-degenerate VBM and CBm at Γ. Its energy, E_{1-4}, lies about 31 meV below the electronic bandgap, as reported in Table 2, indicating a sizable binding energy that remains relevant up to room temperature. The comparatively large binding energy in 2H-Ge can be rationalized within a Wannier–Mott picture, considering that the electron–hole mass along the c axis is substantially larger than in 3C-Ge, and that the 2H phase exhibits slightly lower optical dielectric constants, computed to be $\varepsilon_{\perp c} = 14.35$, $\varepsilon_{\parallel c} = 14.84$, in

21951071, 0, Downloaded from https://advanced.onlinelibrary.wiley.com/doi/10.1002/adom.71234 by CochraneItalia, Wiley Online Library on [16/05/2026]. See the Terms and Conditions (https://onlinelibrary.wiley.com/terms-and-conditions) on Wiley Online Library for rules of use; OA articles are governed by the applicable Creative Commons License

TABLE 2 | Energies of the four degenerate lowest-energy exciton states, E_{1-4} (eV), and maximum oscillator-strength values (dimensionless), computed via Equation (2), among the degenerate states for the two light polarizations.

	E_{1-4}	$f^{\max}_{1-4,\perp c}$	$f^{\max}_{1-4,\parallel c}$
2H-Ge	0.289	$6.61 \cdot 10^{-9}$	$2.19 \cdot 10^{-15}$
2H-Ge $\epsilon_z = 2\%$	0.295	$3.99 \cdot 10^{-4}$	$1.15 \cdot 10^{-14}$
2H-$\mathrm{Si}_{1/6}\mathrm{Ge}_{5/6}$	0.568	$1.59 \cdot 10^{-6}$	$7.73 \cdot 10^{-8}$
2H-$\mathrm{Si}_{1/4}\mathrm{Ge}_{3/4}$	0.546	$1.80 \cdot 10^{-6}$	$8.57 \cdot 10^{-8}$
2H-$\mathrm{Si}_{1/2}\mathrm{Ge}_{1/2}$	0.962	$7.08 \cdot 10^{-6}$	$6.64 \cdot 10^{-8}$
GaN	3.322	$3.41 \cdot 10^{-3}$	$5.61 \cdot 10^{-10}$

comparison to $\varepsilon = 15.8$ in 3C-Ge [47]. These factors naturally account for the stronger exciton binding in 2H-Ge compared to the 3C phase. This justifies the explicit inclusion of electron–hole interactions via the BSE and the analysis of intrinsically excitonic quantities such as dipole moments and radiative lifetimes. The dipole moments of the four degenerate lowest-energy excitons for in-plane polarization range from 10^{-10} to 10^{-7} a_0^2, whereas for out-of-plane polarization they are several orders of magnitude smaller. These states are therefore dark for light polarized $\parallel c$ and only weakly active for $\perp c$ polarization. For comparison, Figure 3f reports the corresponding $|\mu_{S,\alpha}|^2$ values for GaN, a well-known efficient light emitter: its in-plane dipole moments reach values up to 10^{-1} a_0^2, more than six orders of magnitude larger than those of 2H-Ge. This confirms that radiative emission in 2H-Ge is not only strongly in-plane polarized but also intrinsically very weak. Consistently, the absorption spectrum of 2H-Ge shows no noticeable structure at the band edge, in agreement with previous calculations [6], reflecting the extremely small dipole moment of the lowest exciton. The corresponding dimensionless oscillator strength, evaluated according to Equation (2) and therefore incorporating both the dipole moment and the exciton energy, reaches a maximum value of $6.61 \cdot 10^{-9}$ for in-plane polarized light (Table 2). Only above ~0.5 eV a visible feature appears in the spectrum, followed by a steady increase beyond 1 eV, driven by strong transitions involving the VBM and the CBm+1 states.

The picture changes markedly in uniaxially strained 2H-Ge, Figure 3b. As discussed above, the band crossover activates much stronger transitions from the VBM (Γ^+_{9v}) to the new CBm (Γ^-_{7c}), which now dominate the lowest-energy excitons. The dipole moments for $\parallel c$ polarization are only weakly affected, whereas those for $\perp c$ polarization increase by more than five orders of magnitude relative to the unstrained material. Under $\epsilon_z = 2\%$ strain, the lowest-energy excitons reach dipole moments around 10^{-1} a_0^2, comparable to GaN. In contrast to the unstrained case, the absorption spectrum now exhibits a clear feature at the band edge before following the same overall trend as pristine 2H-Ge and increasing steadily at higher energies. The maximum oscillator strength accordingly reaches $3.99 \cdot 10^{-4}$ for $\perp c$ polarization (Table 2). This confirms that applying about 2% uniaxial strain along the c axis substantially enhances the light-matter interactions of 2H-Ge through the strain-induced band crossover.

The alloy systems, shown in Figure 3c–e, all exhibit a slow onset of absorption starting above ~0.5 eV and reaching only about one tenth of the intensity observed in pristine and strained 2H-Ge around 1.5 eV (cf. the vertical scales in panels (a)–(e)). The absorption increases more slowly with increasing Si content. Spectral features that are visible for $x = {}^1\!/_6$ above 1 eV for $\perp c$ polarization become increasingly suppressed at higher Si concentrations and eventually disappear. This trend originates from the pronounced progressive upward shift of the CBm+1 state at the Γ point, see Figure 2c–e, which pushes the strong optical transitions driving the absorption to significantly higher energies than in the 2H-Ge systems. Alloying also markedly reduces the contrast between in-plane and out-of-plane dipole strengths. For both polarizations, the exciton dipole moments span the range 10^{-7} – 10^{-4} a_0^2, with the lowest-energy states reaching values of order 10^{-4} a_0^2 for $\perp c$ and 10^{-5} a_0^2 for $\parallel c$. This behavior is consistent across the different Si concentrations considered here, with comparable dipole-moment magnitudes observed throughout the explored composition range. The symmetry breaking introduced by the random distribution of Si atoms lifts the suppression of the $\parallel c$ dipole component present in pristine 2H-Ge. As a result, the alloys exhibit optical responses that are nearly isotropic with respect to light polarization, with comparable dipole strengths for the $\perp c$ and $\parallel c$ directions. We note that this effect may be enhanced by the finite size of the alloy supercells considered here, where the reduced symmetry of a single representative configuration can partially overestimate polarization mixing compared to the macroscopic random-alloy limit. The corresponding oscillator strengths of the lowest-energy states fall between the very small values found in pristine 2H-Ge and the significantly larger values characteristic of uniaxially strained 2H-Ge.

The results for our GaN comparison are shown in Figure 3f. The binding energy of the lowest-energy, fourfold-degenerate excitons is larger than in the 2H-Ge–based systems, in agreement with previous calculations [48]. As noted earlier, GaN is an efficient light-emitting semiconductor and, correspondingly, the in-plane exciton dipole moments are of order 10^{-1} a_0^2, whereas the out-of-plane components are about seven orders of magnitude smaller. The combination of these large $\perp c$ dipole moments with the substantially higher exciton energy $E_{1-4} = 3.322$ eV yields oscillator strengths that exceed those of strained 2H-Ge by approximately one order of magnitude, reaching $3.41 \cdot 10^{-3}$ along the $\perp c$ direction (Table 2).

3.3 | Exciton Radiative Lifetimes

From the exciton dipole moments along the two polarization directions, and using Equations (3) and (4), we compute the thermally averaged radiative lifetimes $\langle\tau\rangle(T)$ of the studied systems, shown in Figure 4. The left panel reports the temperature dependence of $\langle\tau\rangle(T)$ for the different materials, while the right panel compares the average lifetimes evaluated at $T = 10$ K. The 2H-$\mathrm{Si}_{1/2}\mathrm{Ge}_{1/2}$ alloy is not considered, as its electronic bandgap is indirect and the lowest-energy exciton is indirect, rendering radiative recombination momentum-forbidden.

All lifetimes reported here are computed in the intrinsic limit, i.e., in the absence of doping or free carriers, so that excitons remain stable and unscreened throughout the temperature range and no extrinsic recombination channels or many-body screening effects alter the radiative dynamics.

21951071, 0, Downloaded from https://advanced.onlinelibrary.wiley.com/doi/10.1002/adom.71234 by CochraneItalia, Wiley Online Library on [16/05/2026]. See the Terms and Conditions (https://onlinelibrary.wiley.com/terms-and-conditions) on Wiley Online Library for rules of use; OA articles are governed by the applicable Creative Commons License

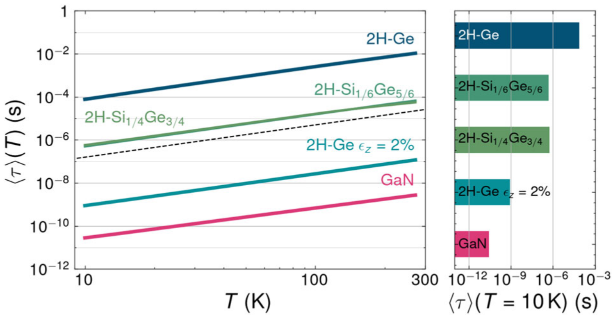

FIGURE 4 | Temperature-averaged exciton radiative lifetimes, Equation (4), of the studied materials. Left panel, from top to bottom: temperature dependence of $\langle\tau\rangle(T)$ for pristine 2H-Ge, 2H-$Si_{1/6}Ge_{5/6}$, and 2H-$Si_{1/4}Ge_{3/4}$ alloys, uniaxially strained 2H-Ge and GaN. The dashed black line shows an exact $T^{3/2}$ trend. Right panel: comparison of the materials' average radiative lifetimes at $T = 10$ K.

Across all materials, the average lifetimes follow the $T^{3/2}$ scaling, indicated by the dashed black line in the left panel of Figure 4, with remarkable accuracy. This behavior reflects the fact that, up to room temperature, the radiative dynamics are governed almost entirely by the fourfold-degenerate lowest-energy excitons. In all 2H-Ge–based systems, the next excitonic states lie more than 45 meV higher in energy and therefore remain essentially unpopulated over the explored temperature range. As a result, the thermal average in Equation (4) reduces to the contribution of these four states alone, without any progressive activation of higher excitons. The temperature dependence of $\langle\tau\rangle(T)$ therefore arises solely from the T dependence of the single-state lifetime $\tau_S(T)$, i.e., from the thermal factor in Equation (3), leading to the characteristic $T^{3/2}$ scaling.

Pristine 2H-Ge exhibits the longest radiative lifetime among all materials considered, already exceeding by two orders of magnitude the microsecond scale at low temperature. This originates from the exceptionally small exciton dipole moments for both polarization directions and confirms the very low light-emission efficiency of hexagonal germanium. If the electron–hole interaction is neglected, i.e., by switching off the direct and exchange terms in the BSE kernel, while still enforcing momentum conservation within the light cone, the resulting radiative lifetime increases by roughly a factor two, as shown in Figure S4.

Although the excitonic and the fully IP regimes represent fundamentally different physical pictures, a comparison remains useful. At low temperatures ($\sim$10 K), the excitonic radiative lifetime obtained here agrees well with the IP values reported in refs. [4, 17], both being of order 10^{-4} s. This correspondence arises because, in this regime, only the lowest degenerate exciton is thermally occupied and its CMM remains extremely close to zero. The exciton wavefunction is largely dominated by a single interband transition at Γ, and radiative recombination effectively reduces to the same vertical transition captured in the IP picture. As mentioned in Section 2, at higher temperatures, however, the two descriptions diverge due to the different treatment of momentum conservation in radiative recombination that is employed: in the excitonic case, the thermal occupation of finite-momentum excitons, together with the light-cone constraint, leads to the characteristic $T^{3/2}$ increase of the radiative lifetime, whereas in the IP picture the thermal population of higher-energy vertical transitions causes a reduction of the radiative lifetime, since the light-cone constraint is not explicitly enforced.

The increase in exciton dipole moments induced by alloying with Si leads to a reduction of the radiative lifetime by roughly two orders of magnitude, bringing it down to the microsecond range at $T \sim 10$ K for both the 2H-$Si_{1/6}Ge_{5/6}$ and 2H-$Si_{1/4}Ge_{3/4}$ alloys (see the right panel of Figure 4). Correspondingly, their $\langle\tau\rangle(T)$ values overlap in the left panel of Figure 4, indicating that no substantial difference in radiative efficiency emerges at these alloy compositions. A much stronger reduction is achieved through the application of uniaxial strain along the c axis. Under $\epsilon_z = 2\%$ strain, the average radiative lifetime decreases by about five orders of magnitude compared to pristine 2H-Ge, reaching the nanosecond scale at low temperature. This reduction directly reflects the bright in-plane transitions enabled by the strain-induced band crossover, placing strained 2H-Ge within technologically relevant emission timescales.

The radiative lifetime of strained 2H-Ge remains, however, about one order of magnitude longer than that of our GaN benchmark, which reaches $\sim$30 ps at 10 K, in excellent agreement with the literature [40, 49]. Although the exciton dipole moments for $\perp c$ polarization are of similar magnitude in strained 2H-Ge and GaN, the shorter GaN lifetime originates from its much larger exciton energy: the energy of the degenerate lowest states in GaN is nearly an order of magnitude higher, which directly amplifies the oscillator strength (cf. Table 2) and correspondingly reduces the radiative lifetime, see Equation (3).

4 | Summary and Conclusion

In this work, we present a comprehensive excitonic analysis of pristine 2H-Ge and of its alloyed and strained variants, using wurtzite GaN as reference. By combining ab initio DFT + J electronic structures with BSE calculations, we quantify the exciton binding energies, dipole moments, and intrinsic radiative lifetimes of these systems.

Across all 2H-Ge–based materials studied, the sizeable binding energies demonstrate that excitonic effects remain relevant well above cryogenic temperatures and must be explicitly included to capture the optical response. The fourfold-degenerate excitons at the band edge dominate the radiative dynamics up to room temperature, leading to the characteristic $T^{3/2}$ dependence of the average radiative lifetime.

Our results show that pristine 2H-Ge possesses exceptionally small exciton dipole moments for both in-plane and out-of-plane light polarization, resulting in very long radiative lifetimes exceeding 10^{-4} s at low temperature. This confirms the intrinsically weak optical activity of hexagonal Ge and is consistent with the absence of strong spectral features near the band edge reported experimentally.

Alloying Ge with Si moderately increases the dipole strength and reduces the radiative lifetime, primarily due to the lifted constraints on optical transitions. A much more pronounced

21951071, 0, Downloaded from https://advanced.onlinelibrary.wiley.com/doi/10.1002/adom.71234 by CochraneItalia, Wiley Online Library on [16/05/2026]. See the Terms and Conditions (https://onlinelibrary.wiley.com/terms-and-conditions) on Wiley Online Library for rules of use; OA articles are governed by the applicable Creative Commons License

enhancement arises under uniaxial strain along the c axis, where the strain-induced band crossover activates strong in-plane transitions, yielding dipole moments, and radiative efficiencies comparable to those of GaN. Under $\epsilon_z = 2\%$ strain, the radiative lifetime reaches the nanosecond regime, with a five-orders of magnitude improvement over pristine 2H-Ge.

Taken together, our results provide an additional investigation on the intrinsic optical response of 2H-Ge, reinforcing earlier theoretical indications of a mismatch between its band-edge properties and the strong PL reported in some experiments. The very weak exciton dipoles and long intrinsic lifetimes obtained here support the view that the observed PL is likely mediated by extrinsic channels, such as defects, morphology, or local strain fields, rather than by the radiative recombination of a bright exciton. Conversely, our results identify strain engineering as a highly effective route to enhance intrinsic emission in hexagonal Ge, far more efficient than alloying.

Overall, this work fills a gap in the current understanding of hexagonal Ge by providing a microscopic excitonic perspective on its radiative properties and offering additional quantitative evidence that clarifies the intrinsic limits of light emission in this polytype.

Acknowledgements

M.R.F. and M.P. thank Ivan Marri and Sudha Priyanga Ganesapandian for helpful discussions. M.R.F. and M.P. acknowledge the "Italian Research Center on High Performance Computing, Big Data, and Quantum Computing" (ICSC) funded by the European Union-NextGenerationEU and established under the National Recovery and Resilience Plan (PNRR), as well as high-performance computing resources provided by CINECA through the ISCRA initiative. M.A. acknowledges the ANR AMPHORE project (ANR-21-CE09-0007) and the ANR TULIP (ANR-24-CE09-5076). MP thanks INFN for the TIME2QUEST funding project.

Open access publishing facilitated by Politecnico di Torino, as part of the Wiley - CRUI-CARE agreement.

Conflicts of Interest

The authors declare no conflicts of interest.

Data Availability Statement

The data that supports the findings of this study are available in the supplementary material of this article.

References

1. L. S. Ramsdell, "Studies on Silicon Carbide," *American Mineralogist* 32, no. 1–2 (1947): 64–82.

2. H. I. T. Hauge, S. Conesa-Boj, M. A. Verheijen, S. Koelling, and E. P. A. M. Bakkers, "Single-Crystalline Hexagonal Silicon–Germanium," *Nano Letters* 17, no. 1 (2017): 85–90.

3. L. Vincent, G. Patriarche, G. Hallais, et al., "Novel Heterostructured Ge Nanowires Based on Polytype Transformation," *Nano Letters* 14, no. 8 (2014): 4828–4836.

4. E. M. T. Fadaly, A. Dijkstra, J. R. Suckert, et al., "Direct-Bandgap Emission from Hexagonal Ge and SiGe Alloys," *Nature* 580, no. 7802 (2020): 205–209.

5. A. Li, H. I. T. Hauge, M. A. Verheijen, et al., "Hexagonal Silicon–Germanium Nanowire Branches with Tunable Composition," *Nanotechnology* 34, no. 1 (2022): 015601.

6. L. H. G. Tizei, M. R. Fiorentin, T. Dursap, et al., "Optical Absorption in Hexagonal-Diamond Si and Ge Nanowires: Insights from STEM-EELS Experiments and Ab Initio Theory," *Nano Letters* 25, no. 21 (2025): 8604–8611.

7. D. Lamon, H. A. J. van der Donk, M. A. Verheijen, M. M. Jansen, and E. P. A. M. Bakkers, "Dimension Control of Hexagonal SiGe Single-Branched Nanowires," *Nano Letters* 25, no. 14 (2025): 5741–5746.

8. W. H. J. Peeters, V. T. van Lange, A. Belabbes, et al., "Direct Bandgap Quantum Wells in Hexagonal Silicon Germanium," *Nature Communications* 15, no. 1 (2024): 5252.

9. W. H. J. Peeters, M. M. Jansen, M. F. Schouten, et al., "Growth Rate of Hexagonal SiGe Multi-Quantum Wells," *Physical Review B* 111, no. 24 (2025): L241302.

10. R. Soref, "The Past, Present, and Future of Silicon Photonics," *IEEE Journal of Selected Topics in Quantum Electronics* 12, no. 6 (2006): 1678–1687.

11. R. Soref, "Mid-Infrared Photonics in Silicon and Germanium," *Nature Photonics* 4, no. 8 (2010): 495–497.

12. F. Priolo, T. Gregorkiewicz, M. Galli, and T. F. Krauss, "Silicon Nanostructures for Photonics and Photovoltaics," *Nature Nanotechnology* 9, no. 1 (2014): 19–32.

13. D. Thomson, A. Zilkie, J. E. Bowers, et al., "Roadmap on Silicon Photonics," *Journal of Optics* 18, no. 7 (2016): 073003.

14. M. A. J. van Tilburg, W. H. J. Peeters, M. Vettori, V. T. van Lange, E. P. A. M. Bakkers, and J. E. M. Haverkort, "Polarized Emission from Hexagonal Silicon–Germanium Nanowires," *Journal of Applied Physics* 133, no. 6 (2023): 065702.

15. V. T. van Lange and A. Dijkstra, and E. M. T. Fadaly, "Nanosecond Carrier Lifetime of Hexagonal Ge," *ACS Photonics* 11, no. 10 (2024): 4258–4267.

16. C. Rödl, J. Furthmüller, J. R. Suckert, V. Armuzza, F. Bechstedt, and S. Botti, "Accurate Electronic and Optical Properties of Hexagonal Germanium for Optoelectronic Applications," *Physical Review Materials* 3, no. 3 (2019): 034602.

17. J. R. Suckert, C. Rödl, J. Furthmüller, F. Bechstedt, and S. Botti, "Efficient Strain-Induced Light Emission in Lonsdaleite Germanium," *Physical Review Materials* 5, no. 2 (2021): 024602.

18. P. Borlido, F. Bechstedt, S. Botti, and C. Rödl, "Ensemble Averages of Ab Initio Optical, Transport, and Thermoelectric Properties of Hexagonal $\mathrm{Si}_x\mathrm{Ge}_{1-x}$ Alloys," *Physical Review Materials* 7, no. 1 (2023): 014602.

19. A. Belabbes, F. Bechstedt, and S. Botti, "Giant Optical Oscillator Strengths in Perturbed Hexagonal Germanium," *Physica Status Solidi (RRL) – Rapid Research Letters* 16, no. 4 (2022): 2100555.

20. F. Rovaris, W. H. J. Peeters, A. Marzegalli, et al., "2H–Si/Ge for Group-IV Photonics: On the Origin of Extended Defects in Core–Shell Nanowires," *ACS Applied Nano Materials* 7, no. 8 (2024): 9396–9402.

21. O. Madelung, *Semiconductors: Data Handbook* (Springer Science & Business Media, 2004).

22. K. Guilloy, N. Pauc, A. Gassenq, P. Gentile, S. Tardif, F. Rieutord, and V. Calvo, "Tensile Strained Germanium Nanowires Measured by Photocurrent Spectroscopy and X-Ray Microdiffraction," *Nano Letters* 15, no. 4 (2015): 2429–2433.

23. H. Zhang, J. Tersoff, S. Xu, et al., "Approaching the Ideal Elastic Strain Limit in Silicon Nanowires," *Science Advances* 2, no. 8 (2016): e1501382.

24. P. Giannozzi, S. Baroni, N. Bonini, et al., "Quantum ESPRESSO: A Modular and Open-Source Software Project for Quantum Simulations of Materials," *Journal of Physics: Condensed Matter* 21, no. 39 (2009): 395502.

21951071, 0, Downloaded from https://advanced.onlinelibrary.wiley.com/doi/10.1002/adom.71234 by CochraneItalia, Wiley Online Library on [16/05/2026]. See the Terms and Conditions (https://onlinelibrary.wiley.com/terms-and-conditions) on Wiley Online Library for rules of use; OA articles are governed by the applicable Creative Commons License

25. P. Giannozzi, O. Andreussi, T. Brumme, et al., “Advanced Capabilities for Materials Modelling with Quantum ESPRESSO,” *Journal of Physics: Condensed Matter* 29, no. 46 (2017): 465901.

26. P. Giannozzi, O. Baseggio, P. Bonfà, et al., “Quantum ESPRESSO toward the Exascale,” *Journal of Chemical Physics* 152, no. 15 (2020): 154105.

27. J. P. Perdew, A. Ruzsinszky, G. I. Csonka, et al., “Restoring the Density-Gradient Expansion for Exchange in Solids and Surfaces,” *Physical Review Letters* 100, no. 13 (2008): 136406.

28. A. Zunger, S.-H. Wei, L. G. Ferreira, and J. E. Bernard, “Special Quasirandom Structures,” *Physical Review Letters* 65, no. 3 (1990): 353–356.

29. A. van de Walle, P. Tiwary, M. de Jong, et al., “Efficient Stochastic Generation of Special Quasirandom Structures,” *Calphad* 42 (2013): 13–18.

30. A. I. Liechtenstein, V. I. Anisimov, and J. Zaanen, “Density-Functional Theory and Strong Interactions: Orbital Ordering in Mott-Hubbard Insulators,” *Physical Review B* 52, no. 8 (1995): R5467–R5470.

31. A. Georges, L. de’ Medici, and J. Mravlje, “Strong Correlations from Hund’s Coupling,” *Annual Review of Condensed Matter Physics* 4, no. 1 (2013): 137–178.

32. J. Heyd, G. E. Scuseria, and M. Ernzerhof, “Hybrid Functionals Based on a Screened Coulomb Potential,” *Journal of Chemical Physics* 118, no. 18 (2003): 8207–8215.

33. A. De and C. E. Pryor, “Electronic Structure and Optical Properties of Si, Ge, and Diamond in the Lonsdaleite Phase,” *Journal of Physics: Condensed Matter* 26, no. 4 (2014): 045801.

34. T. Kaewmaraya, L. Vincent, and M. Amato, “Accurate Estimation of Band Offsets in Group IV Polytype Junctions: A First-Principles Study,” *Journal of Physical Chemistry C* 121, no. 10 (2017): 5820–5828.

35. A. Marini, C. Hogan, M. Grüning, and D. Varsano, “Yambo: An Ab Initio Tool for Excited-State Calculations,” *Computer Physics Communications* 180, no. 8 (2009): 1392–1403.

36. D. Sangalli, A. Ferretti, H. Miranda, et al., “Many-Body Perturbation Theory Calculations Using the Yambo Code,” *Journal of Physics: Condensed Matter* 31, no. 32 (2019): 325902.

37. D. Sangalli, C. Attaccalite, M. Grüning, et al., “Lumen Code,” accessed December 12, 2025, https://www.lumen-code.org.

38. H.-Y. Chen, V. A. Jhalani, M. Palummo, and M. Bernardi, “Ab Initio Calculations of Exciton Radiative Lifetimes in Bulk Crystals, Nanostructures, and Molecules,” *Physical Review B* 100, no. 7 (2019): 075135.

39. V. A. Jhalani, H.-Y. Chen, M. Palummo, and M. Bernardi, “Precise Radiative Lifetimes in Bulk Crystals from First Principles: The Case of Wurtzite Gallium Nitride,” *Journal of Physics: Condensed Matter* 32, no. 8 (2020): 084001.

40. L. D. Whalley, “Effmass: An Effective Mass Package,” *Journal of Open Source Software* 3, no. 28 (2018): 797.

41. M. Palummo, M. Bernardi, and J. C. Grossman, “Exciton Radiative Lifetimes in Two-Dimensional Transition Metal Dichalcogenides,” *Nano Letters* 15, no. 5 (2015): 2794–2800.

42. C. A. Broderick, X. Zhang, M. E. Turiansky, and C. G. V. de Walle, “First-Principles Theory of Direct-Gap Optical Emission in Hexagonal Ge and Its Enhancement via Strain Engineering,” *arXiv Preprint* (2024), https://arxiv.org/abs/2412.08865.

43. C. Delerue, G. Allan, and M. Lannoo, “Theoretical Aspects of the Luminescence of Porous Silicon,” *Physical Review B* 48, no. 15 (1993): 11024–11036.

44. R. Mayengbam, C. S. Tan, and W. Fan, “Theoretical Insights into the Amplified Optical Gain of Hexagonal Germanium by Strain Engineering,” *RSC Advances* 13, no. 18 (2023): 11324–11336.

45. Z. Wang, Z. Zhang, S. Liu, J. Robertson, and Y. Guo, “Electronic Properties and Tunability of the Hexagonal SiGe Alloys,” *Applied Physics Letters* 118, no. 17 (2021): 172101.

46. M. Suzuki, T. Uenoyama, and A. Yanase, “First-Principles Calculations of Effective-Mass Parameters of AlN and GaN,” *Physical Review B* 52, no. 11 (1995): 8132–8139.

47. W. C. Dunlap and R. L. Watters, “Direct Measurement of the Dielectric Constants of Silicon and Germanium,” *Physical Review* 92, no. 6 (1953): 1396–1397.

48. R. Laskowski, N. E. Christensen, G. Santi, and C. Ambrosch-Draxl, “Ab Initio Calculations of Excitons in GaN,” *Physical Review B* 72, no. 3 (2005): 035204.

49. J. S. Im, A. Moritz, F. Steuber, V. Härle, F. Scholz, and A. Hangleiter, “Radiative Carrier Lifetime, Momentum Matrix Element, and Hole Effective Mass in GaN,” *Applied Physics Letters* 70, no. 5 (1997): 631–633.

Supporting Information

Additional supporting information can be found online in the Supporting Information section.

Supporting File: adom71234-sup-0001-SuppMat.pdf.

21951071, 0, Downloaded from https://advanced.onlinelibrary.wiley.com/doi/10.1002/adom.71234 by Cochraneltalia, Wiley Online Library on [16/05/2026]. See the Terms and Conditions (https://onlinelibrary.wiley.com/terms-and-conditions) on Wiley Online Library for rules of use; OA articles are governed by the applicable Creative Commons License